Hindawi
Journal of Nanotechnology
Volume 2023, Article ID 8858582, 11 pages
https://doi.org/10.1155/2023/8858582

Research Article

Dual-Wavelength Passively Q-Switched Erbium-Doped Fiber Laser Incorporating Calcium Carbonate Nanoparticles as Saturable Absorber

Iman N. Jasem, Hiba H. Abdullah, and Mohammed Jalal Abdulrazzaq

Laser and Optoelectronics Engineering Department, University of Technology-Iraq, Baghdad, Iraq

Correspondence should be addressed to Hiba H. Abdullah; hiba.h.abdullah@uotechnology.edu.iq and Mohammed Jalal Abdulrazzaq; mohammed.j.abdulrazzaq@uotechnology.edu.iq

Received 8 June 2023; Revised 2 September 2023; Accepted 15 September 2023; Published 28 September 2023

Academic Editor: Rajesh Kumar Manavalan

This study experimentally demonstrates the operation of a dual-wavelength passively Q-switched erbium-doped fiber laser that incorporates $CaCO_3$ nanoparticles as a saturable absorber (SA). The SA was prepared by using the drop-casting method, wherein $CaCO_3$ nanoparticles were embedded in a polyvinyl alcohol (PVA) polymer to form a $CaCO_3$/PVA film SA. The film was integrated into a ring laser cavity with a 976 nm pump to generate Q-switched pulses. The properties of the SA were examined experimentally, and its modulation depth is approximately 47%. As the pump power increased from 180 mW to 270 mW and the pulse repetition rate increased from 12.67 kHz to 21.3 kHz, the corresponding pulse width decreased from 35.27 μs to 18.74 μs. The signal-to-noise ratio was approximately 25 dB, highlighting the laser's stability. The results indicate that the proposed $CaCO_3$/PVA SA is suitable for realizing portable Q-switched lasers.

1. Introduction

Recently, there has been significant interest in Q-switched fiber lasers that operate in a microsecond pulse duration [1]. They have a simple setup, are compact and flexible, and produce high-quality beams [2]. These characteristics make them suitable for various applications, including material processing and medical treatments [3, 4]. There are two techniques for implementing Q-switched lasers, active and passive [5]. Generally, the passive technique is favoured over the active technique as it offers multiple advantages [6]. These include the ability to withstand harsh environments, ease of preparation, a smaller physical size, and the lack of a need for complex electronic circuits. Furthermore, the passive approach is more cost-effective [7]. Passive Q-switching pulsed lasers have received significant interest owing to their extensive photonics applications, such as in material processing, optical imaging, and high-speed communication [8]. To convert continuous waves into short energetic pulses, a saturable absorber (SA), a nonlinear optical element, is typically included in the laser cavity [9]. In passive Q-switching, the SA recovery time is longer than the cavity round trip time because the pulse duration is dependent on the time taken to deplete the gain after the SA has reached saturation [10]. The SA is vital in generating stable Q-switching optical pulses, including high-power pulses [11]. SA-based passive Q-switching is considered more dependable than other methods as it offers several benefits, including an uncomplicated cavity design and cost-effectiveness, among others [12]. In the cavity of a fiber laser, the SA or "Q-switcher" exhibits varied optical absorption when pulses of different intensities propagate through it. This can be attributed to the saturable absorption characteristics of SA materials [13]. Various types of functional materials are used to create passively Q-switched pulses. These include semiconductor saturable absorption mirrors (SESAMs) [14], carbon nanotubes (CNTs) [15], graphene [16], transition metal dichalcogenides (TMDs) [17], topological insulators (TIs) [18], antimony films [19], and element oxides [20]. The nanostructure of these materials is an important

area of study in modern science and technology [21]. Moreover, they are in high demand across different engineering fields for application in various systems and designs, such as communication, solar cells, sensors, laser optics, photonic integrated circuits, photonic switching, and optical signal processing [22, 23]. This is because these materials possess unique optical, electronic, magnetic, or mechanical properties. Nanoparticle-based materials exhibit nonlinear absorption effects, such as saturable [24] and multiphoton absorption [25]. These effects are significantly influenced by the type, size, and shape of the nanomaterials [26]. SAs made using these materials typically have a film structure and are affordable, compact, and simple to prepare and handle. Additionally, they exhibit good self-starting behaviour and high compatibility with fiber laser systems [27].

One such nanostructure material is calcium carbonate nanoparticles ($CaCO_3$ NPs) which are referred to as carbonate salt. $CaCO_3$ primarily exists as amorphous $CaCO_3$ (ACC), vaterite, aragonite, and the most thermodynamically stable form, calcite [28]. $CaCO_3$ is highly stable in neutral environmental conditions, making it suitable for various technical applications. Typically, crystalline materials display optically anisotropic properties, which occur when the atoms are not symmetrically arranged in various crystal lattice directions [29]. $CaCO_3$ can be considered a uniaxial crystal. Crystals have interesting optical properties such as double refraction, optical rotation, and polarisation effects. Uniaxial crystals have two components with equal dielectric constants, including trigonal, tetragonal, and hexagonal crystals. Birefringence in uniaxial mediums has many interpretations, producing diverse phenomena, such as the Kerr effect and nonlinear refractive indices. Anisotropic (uniaxial) crystals interact with light differently based on their orientation, resulting in polarised rays with different velocities. The distance between these rays increases with the thickness of the crystal, and their refractive indices are quantified by birefringence [30]. The birefringence of $CaCO_3$ is utilized for technical applications, including in linear polarisers used with high-power lasers [28].

Q-switched fiber lasers that can simultaneously produce multiple wavelengths have several potential applications, such as optical fiber communications, fiber sensing, micromachining, range finding, terahertz generation, and fiber spectroscopy [31, 32]. These lasers generally employ a passive approach with an SA, which is preferred owing to its ease of use and self-starting ability. Although there are various methods for generating dual-wavelength Q-switched fiber lasers, numerous studies have focused on passive approaches using an SA, with different configurations inside the laser cavity for generating different wavelengths [33].

In this study, we propose and demonstrate dual-wavelength passively Q-switched erbium-doped fiber lasers (EDFLs) using $CaCO_3$ NPs as SAs to exploit their saturable absorption properties. The NPs are incorporated into a polyvinyl alcohol (PVA) host to create a $CaCO_3$/PVA film. The film is then incorporated into the cavity of a fiber EDFL to produce a train of Q-switched pulses, with a minimum pulse duration of approximately 18.74 μs. The corresponding pulse energy and pulse repetition rates are 2.861 nJ and 21.3 kHz, respectively. The proposed system can produce a pulsed output with dual wavelengths—1563.5 nm and 1564.9 nm—with a line spacing of approximately 1.4 nm.

2. SA Preparation and Characterization

2.1. $CaCO_3$/PVA SA Fabrication. The fabrication process of the $CaCO_3$/PVA SA is shown in Figure 1. First, a sodium dodecyl sulphate (SDS) solution was prepared by dissolving 1 g of SDS in 100 ml of deionized (DI) water using a magnetic stirrer for 30 min at room temperature. Simultaneously, a PVA solution was prepared by adding 1 g of PVA to 100 ml of DI water, followed by stirring at 60°C for approximately one hour. Subsequently, 2 ml of deionized-sodium dodecyl sulphate (DI-SDS) solution was mixed with 15 mg of $CaCO_3$ powder using a magnetic stirrer for 2 h. Next, 3 ml of PVA solution was added to the $CaCO_3$/SDS solution and stirred for one hour. After stirring, the solution was also ultrasonicated for approximately 45 min to prevent any aggregation. Finally, the obtained suspension was delicately poured into a glass petri dish. The petri dish was allowed to dry naturally at room temperature over four days until a $CaCO_3$/PVA film was formed. The thickness of the prepared film is 53 μm. The entire manufacturing process was conducted in a clean environment.

2.2. Characterisation of $CaCO_3$/PVA SA. NPs are characterized using different techniques to determine their composition, size, morphology, allotropic form, and purity. The crystalline structure of the $CaCO_3$ NPs was measured using continuous scan X-ray diffraction (XRD) with Cu Kα radiation and generator settings of 40 kV and 30 mA from 20° to 80°. The $CaCO_3$ NPs exhibited several diffraction peaks as indicated by their d and θ values. As shown in Figure 2, the most prominent (h k l) peaks were detected at 2θ values of 23.2°, 29.58°, 36.3°, 39.3°, and 43.5°, corresponding to the lattice planes of (1 1 0), (2 0 0), (0 2 0), (1 2 0), and (0 2 2), respectively. $CaCO_3$ is present in calcite form as the d and θ values of the peaks at 29.58° and 43.5° conform to calcite; this also agrees with the result obtained in [34]. The XRD pattern of the $CaCO_3$/PVA film is shown in Figure 3. It was obtained using continuous scan XRD with Cu (1.54060 A°) and generator settings of 40 kV and 30 mA from 10° to 90°. It appears in this form owing to the presence of PVA along with $CaCO_3$ NPs in the precipitation of the $CaCO_3$/PVA SA [35]. Incorporating calcium carbonate into the PVA polymer revealed the lack of a distinct crystalline structure in the composite system. This lack of structure became more pronounced as the concentration of the added salt increased, causing the original crystalline nature of the polymer to diminish. These findings align with previous research in the same field [36]. The alterations in the XRD patterns provided clear evidence of interaction and coordination between the composite components: the polymer and the salt [37].

To further investigate the morphological structure of the $CaCO_3$ crystals which were mainly spherical particles, scanning electron microscope (SEM) images were obtained as shown in Figure 4, with a magnification of ×1300 and ×600. The images

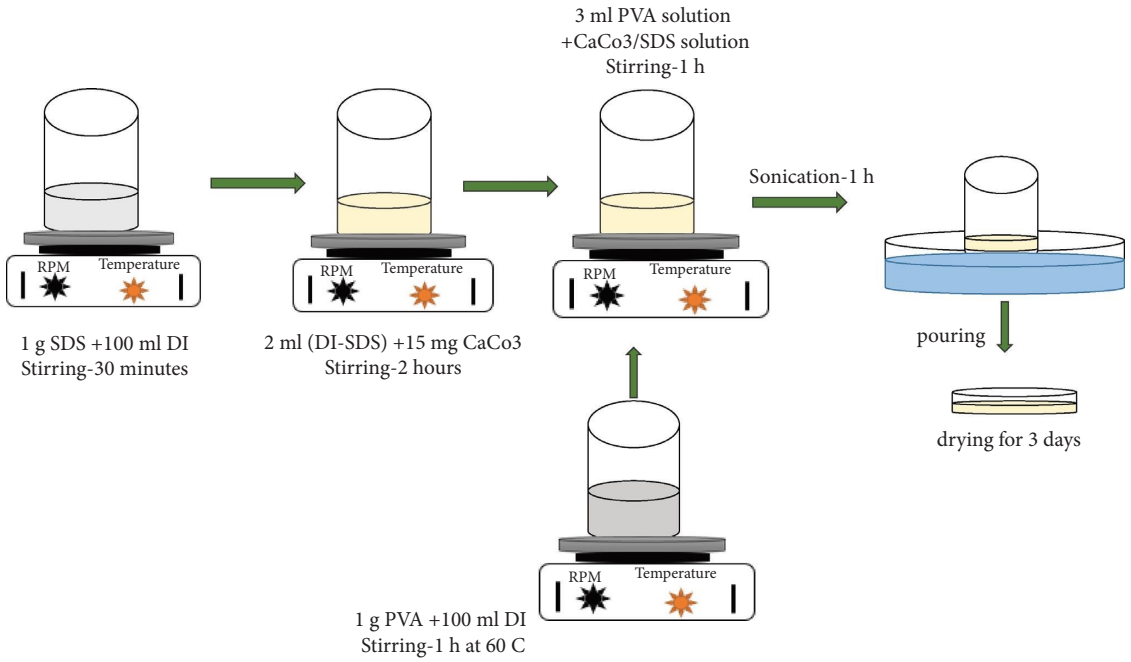

Figure 1: Fabrication of film $CaCO_3$ SA.

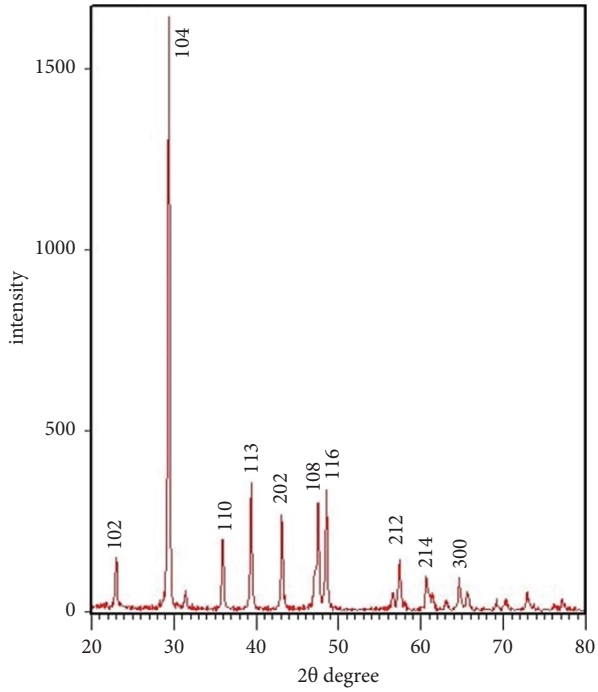

Figure 2: X-ray diffraction (XRD) pattern of $CaCO_3$ NPs.

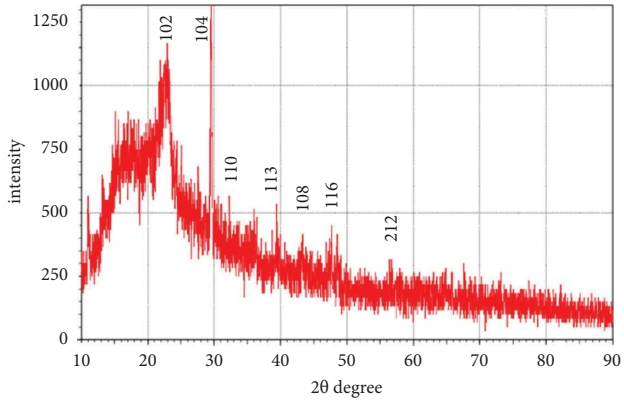

Figure 3: XRD pattern of prepared $CaCO_3$/PVA film.

reveal information about the surface morphology and shape distribution of the $CaCO_3$ NPs. They found that the nanomaterial was formed as a single phase. Additionally, they observed the presence of several aggregates. The nanoparticles exhibited a notable propensity to cluster together and form aggregates, which can be attributed to their elevated surface energy. They are polyhedral and the number of faces changes for different agglomerations of the $CaCO_3$ NPs [38]. Figure 5 shows the SEM images of the $CaCO_3$/PVA film; several particles are fused and form a homogenous film.

Energy dispersive X-ray spectroscopy (EDX) was used to carry out an elemental mapping examination of the $CaCO_3$ NPs considering carbon, oxygen, and calcium. As shown in Figure 6, a small number of impurities exist in the $CaCO_3$ structures. The presence of 0.1 wt.% silicon and 0.3 wt.% magnesium equates to a doping concentration of 0.4 wt.%. The presence of nano-sized magnesium (Mg) with calcium carbonate is as a result of geological and chemical processes, leading to substituting some calcium atoms with magnesium within the compound's structure. This diversity in composition impacts the physical and chemical properties of the compound [39].

Figure 7 shows the chemical composition of the $CaCO_3$ NPs, which is further verified by the elemental mapping images of Ca, C, O, Mg, and Si captured through energy dispersive spectroscopy (EDS).

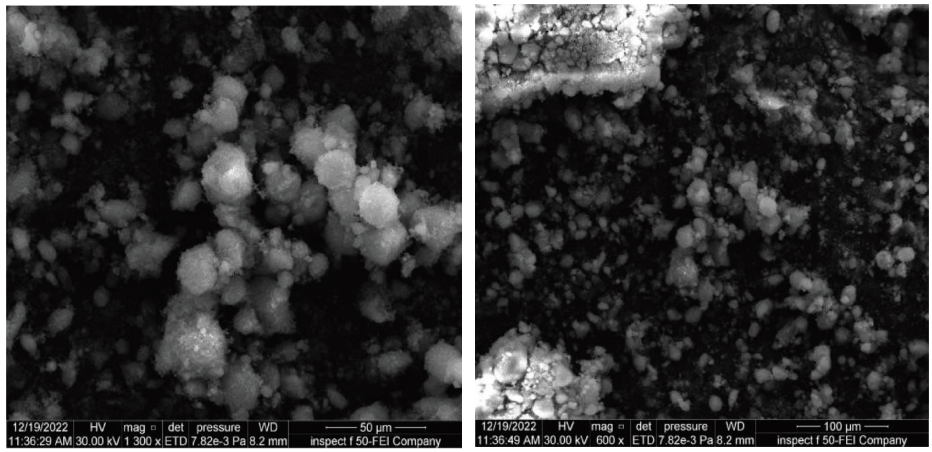

Figure 4: SEM images of $CaCO_3$ NPs.

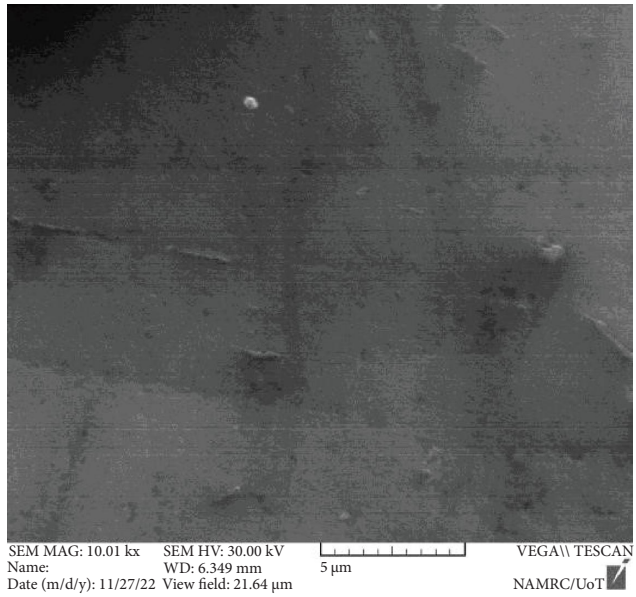

Figure 5: SEM image of $CaCO_3$/PVA film.

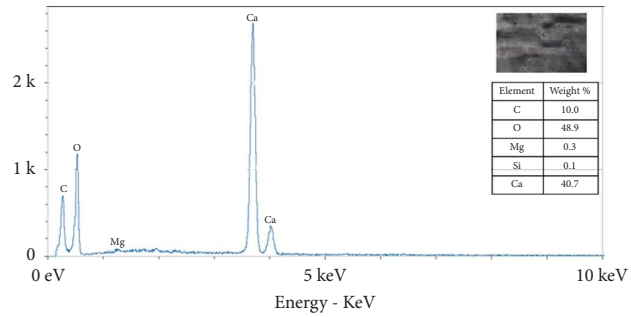

Figure 6: EDX analysis of the $CaCO_3$ NPs.

The optical properties of the $CaCO_3$/PVA film were studied based on its linear absorption spectra and its energy band gap (E_g), which were acquired using a UV–Vis spectrophotometer. An optical spectrum analyzer (OSA) was used to analyze a broad range of low-intensity spectra, ranging from 1520 nm to 1570 nm, produced by a white light source to determine the linear absorption of the $CaCO_3$/PVA SA. The results revealed that the $CaCO_3$/PVA film SA had a linear absorption of approximately 12 dBm at 1561 nm, as shown in Figure 8(a). Figure 8(b) illustrates the UV-visible absorption

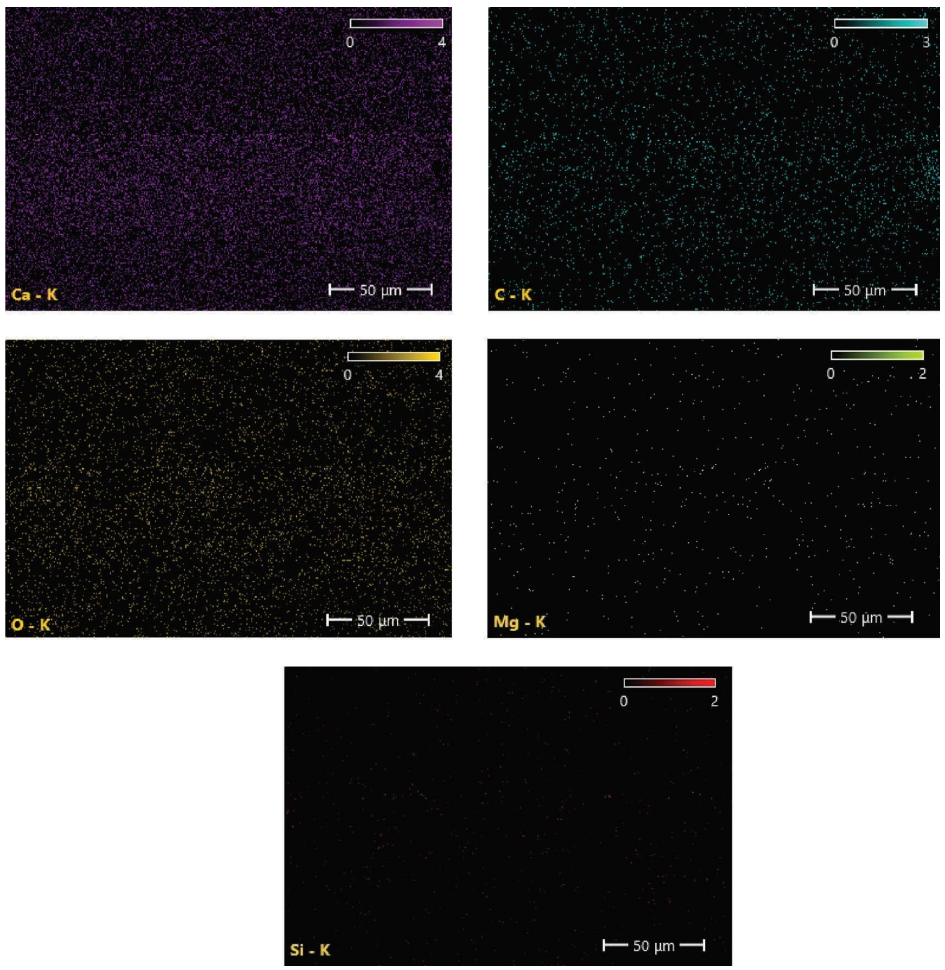

Figure 7: EDS spectra for determining the elemental composition of $CaCO_3$-based passive SA.

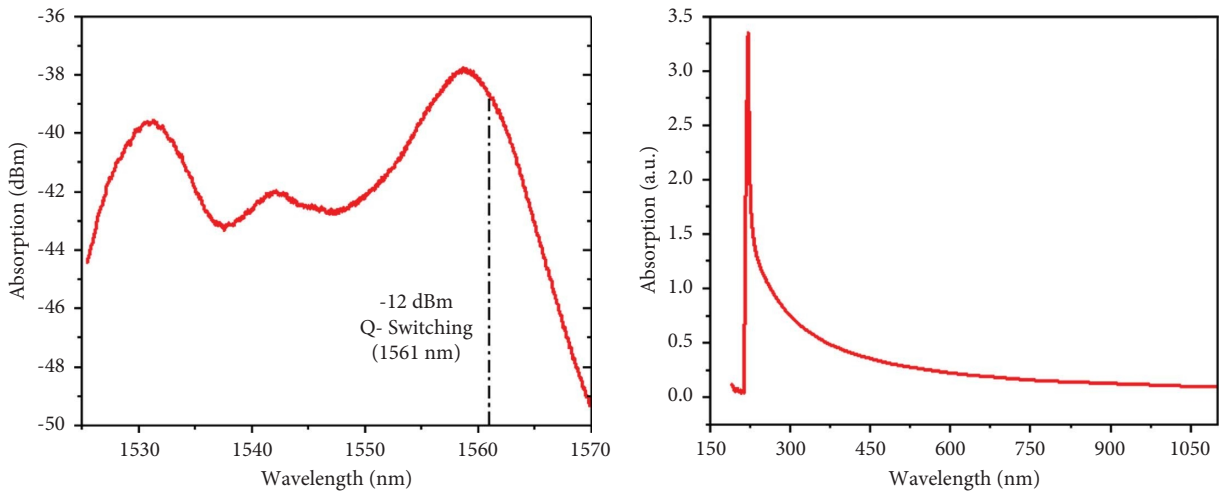

Figure 8: Continued.

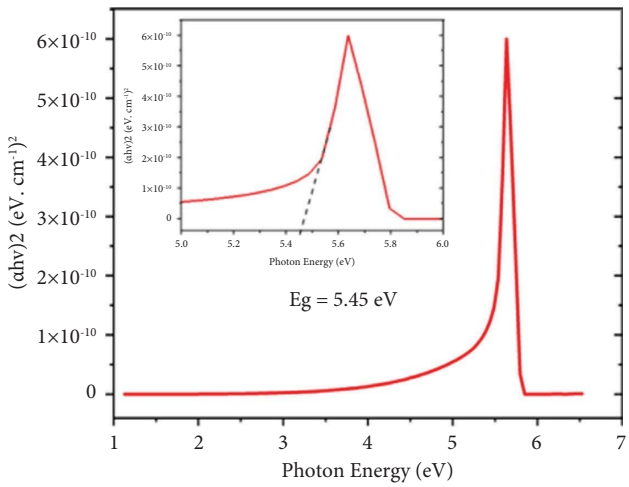

Figure 8: (a) Linear absorption profile of $CaCO_3$ SA, (b) UV-Vis absorption spectrum, and (c) Tauc's plot.

spectrum of a $CaCO_3$/PVA nanocomposite. The band located at 205 indicates the presence of $CaCO_3$ nanoparticles within the nanocomposite [40]. The presence of PVA polymer in the prepared film shows a peak at a wavelength of about 280 nm with a small absorbance of 0.21 [41]. Figure 8(c) shows Tauc's plot of $(\alpha h\nu)^2$ against $h\nu$, extrapolated from the $CaCO_3$/PVA UV–Vis spectrum.

The following equation proposed by Tauc was used to calculate the value of E_g [42]:

$$\alpha h\nu = B\left(h\nu - E_g\right)^n, \quad (1)$$

where α is the absorption coefficient, $h\nu$ is the photon energy, B is a proportional constant, E_g is the optical band gap energy, and $n = 2$ for a direct band gap. The value of E_g can be obtained by extending the linear section of the curve to $(\alpha h\nu)^2 = 0$. The $CaCO_3$ sample has a direct band gap of approximately 5.45 eV.

An IR affinity spectrophotometer was used to verify the phase of the $CaCO_3$ film. The absorption of electromagnetic radiation in the 400–4000 cm^{-1} frequency range generated a Fourier-transform infrared (FTIR) spectrum, as shown in Figure 9. This spectrum revealed vibrational bands at 2918.99 cm^{-1}, 1455.83 cm^{-1}, 874.28 cm^{-1}, and 713.12 cm^{-1}, corresponding to the absorption bands of the in-plane bending (V_4), out-of-plane bending (V_2), and asymmetric stretching (V_3) modes of CO_3^{-2}. The C–O stretching vibrations in PVA are represented by the peaks within the range of 1700 to 1750 cm^{-1}. Additionally, the characteristic peaks of PVA, related to (CH)–CH_2, (OH)–C–OH, and (C–O)–C–OH functional groups, and various other bands within the material are evident in the peaks found between 600 and 1500 cm^{-1} [43]. The characteristic peak of the carbonate group was confirmed through FTIR analysis, which indicated that $CaCO_3$ NPs were present in the prepared $CaCO_3$/PVA film. A sharp peak at 874.28 cm^{-1} demonstrated that the $CaCO_3$ NPs were calcite. Nonetheless, there is a possibility of modest electrostatic attraction occurring between $CaCO_3$ and the –OH group in PVA. This is attributed to the positive electronic nature of Ca in $CaCO_3$

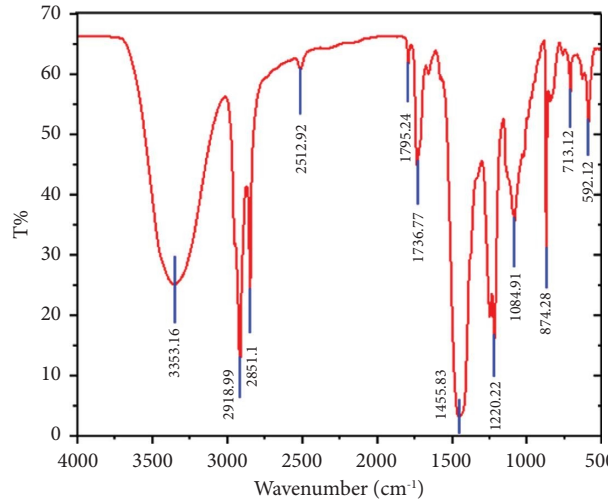

Figure 9: Fourier-transform infrared analysis of $CaCO_3$/PVA film.

and the negative electronic nature of O in –OH, resulting from atomic polarity. However, this interaction is of such subtle strength that it remains undetectable through FTIR analysis [44].

The Z-scan is a technique for determining the nonlinear refractive index and nonlinear absorption coefficient of nonlinear optical materials. The nonlinear optical properties were calculated using a continuous wave (CW) diode pump solid-state laser (DPSSL) with a wavelength of 1064 nm, peak power of 100 mW, and spot size of approximately 2 mm. Figure 10 illustrates the fundamental setup of the Z-scanning technique, along with its optical path. A lens with a 10 cm focal length was used to focus the CW laser beam on the specimen. The sample ($CaCO_3$/PVA film) was fixed on a movable stage along the Z-axis during the experiment to record the relationship between the variation in the Z value and the light intensity. The setup also consists of an aperture with a pinhole diameter of 1 mm and a photodetector to examine the change in the signal.

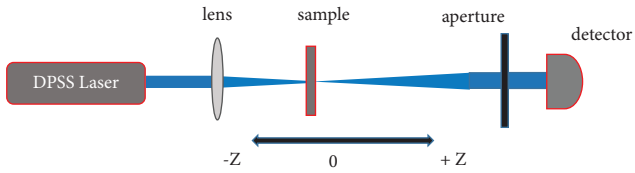

Figure 10: Z-scan experimental setup.

The nonlinear absorption coefficient (β) and nonlinear refractive index (n_2) were calculated using both the open and closed aperture techniques. Figure 11 shows the Z-scan profiles for the closed and open apertures.

The nonlinear optical properties were calculated using the following equations:

$$n_2\,(\text{nonlinear refractive index}) = \frac{\Delta\varnothing_0}{KI_0L_{\text{eff}}}, \tag{2}$$

where $\Delta\varnothing_0$ is the phase shift, K is the wavenumber $(2\pi/\lambda)$, I_0 refers to the laser beam intensity at the focusing point, and L_{eff} is the effective length of the propagation light inside the specimen, $L_{\text{eff}} = 1 - e^{(-L\alpha)}/\alpha$ [45].

$$\beta\,(\text{nonlinear absorption coefficient}) = \frac{2\sqrt{2}\Delta T}{I_0L_{\text{eff}}}, \tag{3}$$

where ΔT is the difference between the maximum and minimum transmission [46].

The results indicate that the nonlinear refractive index, absorption coefficient, and modulation depth of the $CaCO_3$ NPs are 2.8×10^{-6} cm^2/w, 0.189 cm/w, and 47%, respectively.

3. The Ring Cavity Setup

Erbium-doped fiber (EDF) that has a peak core absorption, mode field diameter, and numerical aperture of 80 dB/m at 1530 nm and 9.5 μm at 1550 nm and 0.13, respectively, with a length of 1 m, served as the gain medium. A 976 nm laser diode (LD) (THORLABS- CLD1015) was used to pump the EDF through a 980/1550 nm wavelength division multiplexer (WDM) (THORLABS). To ensure the unidirectional propagation of the oscillating laser, an optical isolator (THORLABS) was included in the ring laser cavity. The $CaCO_3$/PVA film was placed on a clean fiber ferrule with an index-matching gel using an FC/PC connector. The ferrule with the inserted SA was then joined to another clean fiber ferrule using another FC/PC connector. The laser output was obtained through a 90/10 coupler, where 90% of the light continued to oscillate in the cavity, and the remaining 10% was tapped out as the output. The output was detected using an OSA, an optical power meter, and a 2 GHz/s digital storage oscilloscope. Figure 12 illustrates the ring cavity setup.

4. Results and Discussion

The ring laser setup was cleared of all impurities, especially those forming on the fiber connector. Initially, the oscilloscope only indicated CW signals, even when the LD pump power increased to its maximum value. When the SA was inserted into the laser cavity, the CW mode vanished. Once the input power reached the threshold of 180 mW, the Q-switching operation commenced. As the pump power increased to 270 mW, a steady pulse train was observed, which remained within a certain range. Based on the increase in pump power, the variation in the characteristics of the output pulse, such as the repetition rate, pulse width, output power, and pulse energy, were calculated, and the results are shown in Figure 13. Figure 13(a) shows the repetition rate and pulse width of the Q-switched EDFL pulses relative to the pump power. Passively Q-switched lasers exhibit a characteristic pattern wherein the repetition rate decreases as the pulse width increases [47]. In this study, as the pulse width decreased from 35.27 μs to 18.74 μs and the pump power increased from 180 mW to 270 mW, the pulse repetition rate increased from 12.67 kHz to 21.3 kHz. This behaviour is typical for passively Q-switched lasers. Reducing the pump power increases the time required for refilling the extracted energy between successive pulses, leading to a lower repetition rate [48]. If the pump power falls below 180 mW, the Q-switching operation may become unstable, causing noticeable amplitude variations and a decrease in the output power. The instantaneous pulse energy and output power were calculated from the recorded repetition rate and pulse width. Both the output power and pulse energy increased as the pump power was increased from 180 mW to 270 mW. This behaviour is typical for passively Q-switched fiber lasers and conforms to the trend observed in [49].

The results shown in Figure 13(b) indicate that the ring cavity's output power exhibits promising performance when the pump power is 180–270 mW, with a value of 0.044–0.151 mW. These values correspond to a pulse energy of 1.55–2.82 nJ, which is also shown in Figure 13(b).

The Q-switching pulse train of the EDFL at three distinct pump powers, 180 mW, 220 mW, and 270 mW, is illustrated in Figure 14(a). The pulses exhibit a consistent shape, frequency, and pulse width. The figure demonstrates that as the pump power changes, the pulse characteristics, such as the repetition rate and pulse width, also change. As the pump power decreased from 270 mW to 180 mW, a noticeable increase was observed in the duration of the pulse train. Figure 14(b) shows the pulse train of the Q-switched fiber laser, which was acquired using a digital oscilloscope trace with the pump power set at a maximum of 270 mW. Figure 14(b) shows the pulse train, with a pulse width at FWHM of 18.74 μs.

Figure 15(a) depicts the laser output wavelengths for CW (without SA) and Q-switched operations (with SA) at a maximum pump power of 270 mW. The optical spectrum of the EDFL without an SA is shown in Figure 15(a), with a central wavelength of 1561 nm. The output pulse optical spectra are measured at self-started and maximum powers to investigate the impact of the pump power on the generated pulses. Figure 15(b) depicts the laser spectrum with the $CaCO_3$ SA. The laser operates with a dual-wavelength 1563.5 nm and 1564.9 nm at output powers of −14 dBm and −13.2 dBm, respectively. The wavelength separation between the two peaks is 1.4 nm.

As shown in Figure 16, the proposed laser system was evaluated for radio frequency (RF) stability. The results indicate a signal-to-noise ratio (SNR) of 25 dB, which confirms that the output pulse exhibits a stable spectrum

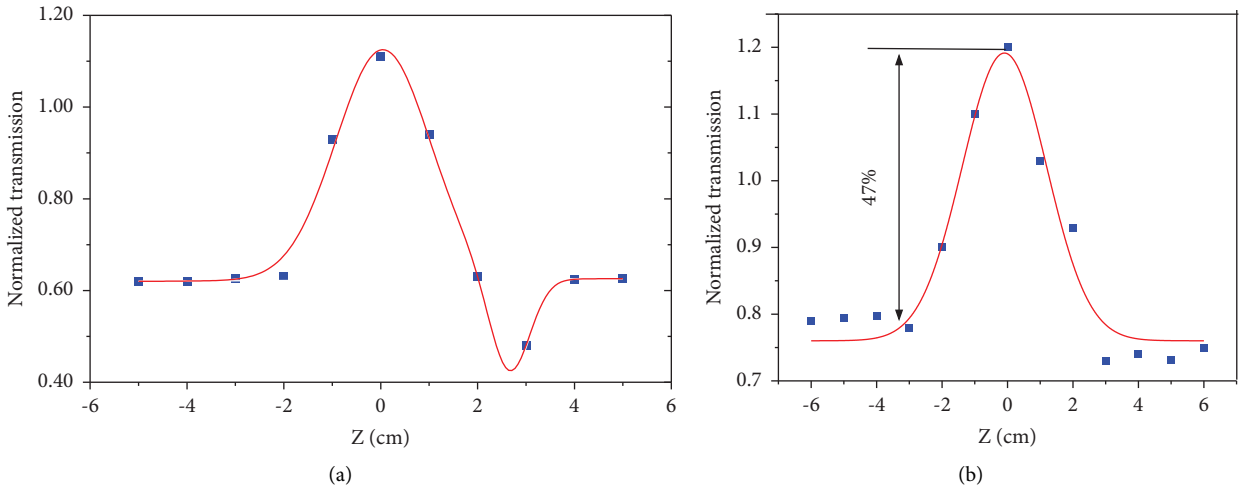

Figure 11: Z-scan profiles with (a) closed aperture and (b) open aperture.

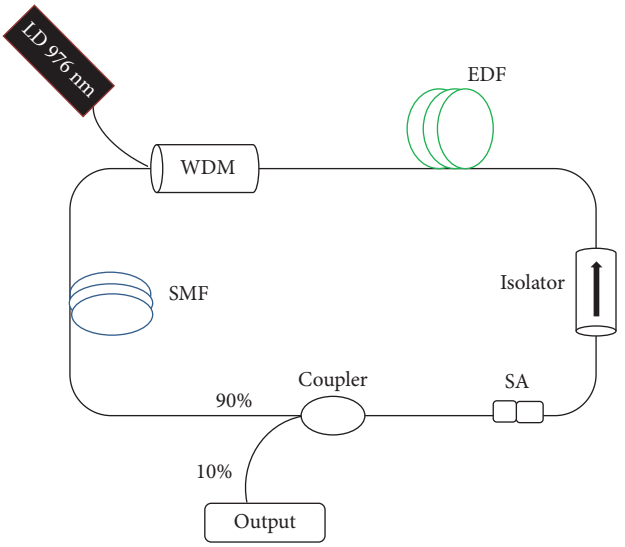

Figure 12: The configuration of the ring laser cavity.

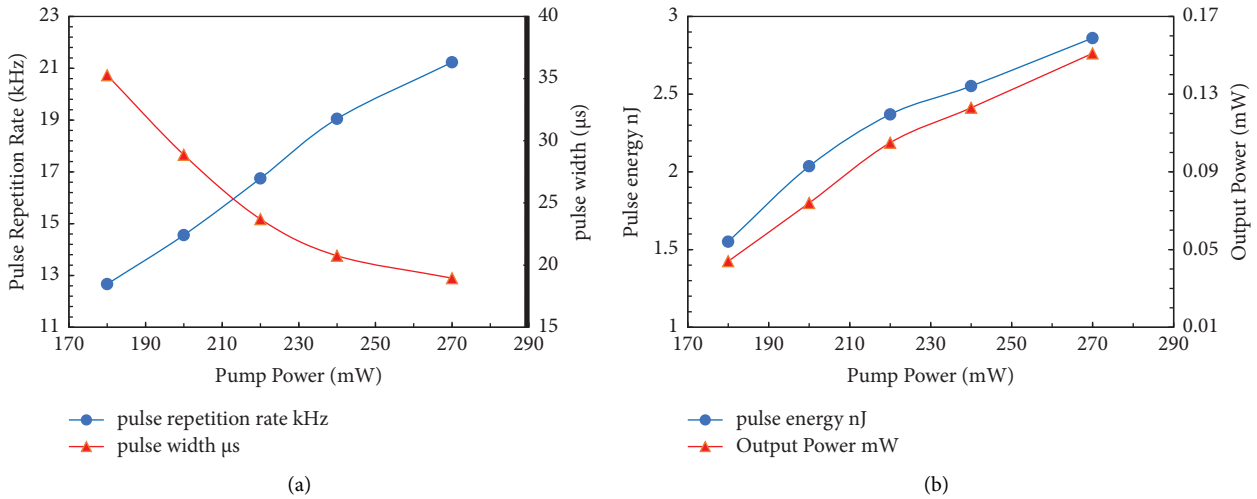

Figure 13: (a) Pulse repetition rate and pulse width vs. pump power and (b) pulse energy and output power vs. pump power.

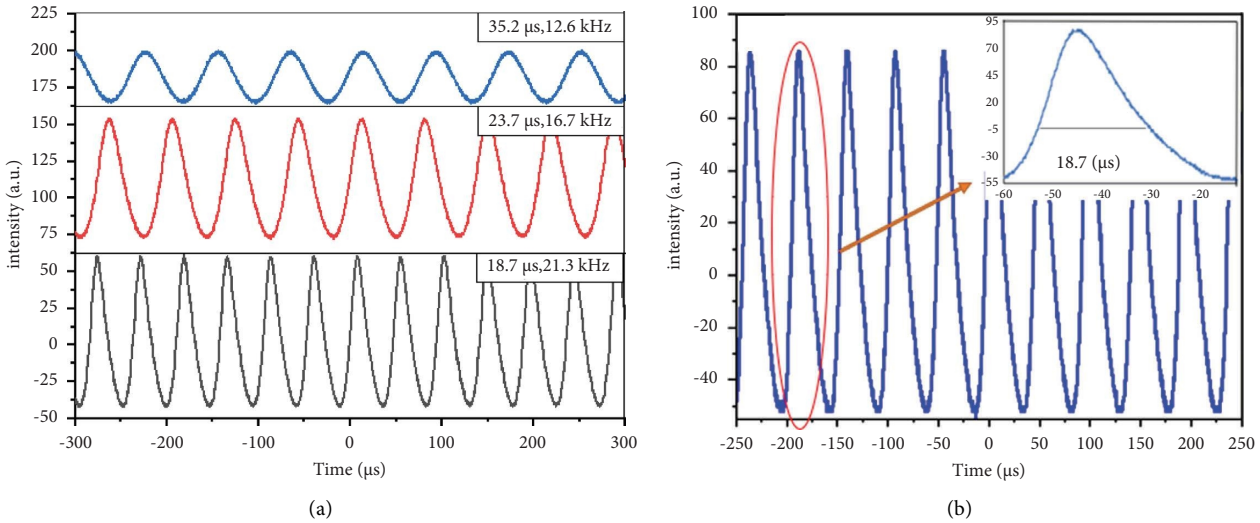

(a) (b)

FIGURE 14: Oscilloscope trace for EDFL with $CaCO_3$ at (a) pump powers of 180 mW, 220 mW, and 270 mW; (b) maximum pump power of 270 mW.

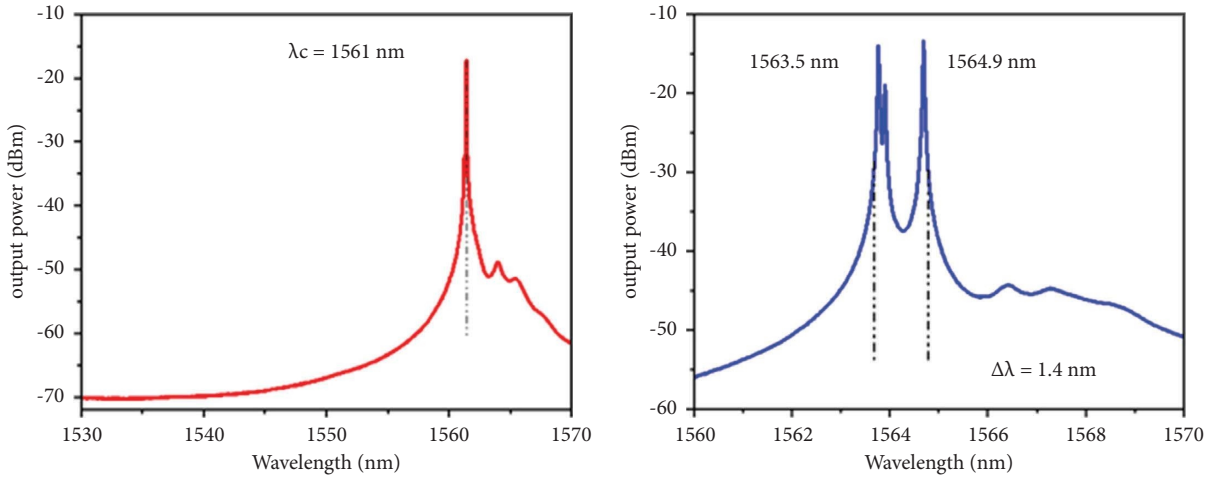

(a) (b)

FIGURE 15: Q-switched EDFL optical spectrum measured at a pump power of 270 mW: (a) without SA and (b) with $CaCO_3$ SA operating at dual wavelengths.

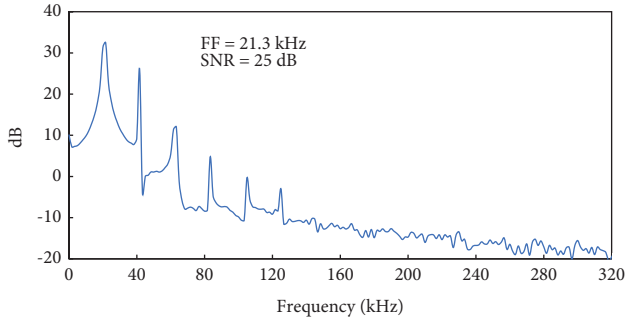

FIGURE 16: Q-switched laser RF spectrum at a pump power of 270 mW.

with $CaCO_3$/PVA as a passive SA, with a maximum repetition rate of 21.3 kHz at a maximum pump power of 270 mW. The stability of the dual Q-switching operation is validated by the observation of the sixth-order harmonics of the specific repetition rate.

5. Conclusions

A $CaCO_3$/PVA SA was successfully fabricated to achieve a dual-wavelength passively Q-switched EDFL. The SA had a modulation depth of 47%. As the repetition rate increased from 12.67 kHz to 21.3 kHz, the pulse widths of the Q-switched laser decreased from 35.27 μs to 18.74 μs. As the pump power increased from 180 mW to 270 mW, the output power increased from 0.044 mW to 0.151 mW, and the pulse energy increased from 1.55 nJ to 2.82 nJ. To the best of our knowledge, this is the first demonstration of a passively Q-switched fiber laser using a $CaCO_3$/PVA film SA. The experimental results indicate that $CaCO_3$ NPs have nonlinear saturation absorption characteristics ($n_2 = 2.8 \times 10^{-6}$ cm^2/w, $\beta = 0.189$ cm/w) and can function as the Q-switcher in high-speed pulsed fiber lasers.

Data Availability

The experimental data used to support the findings of this study are available on request.

Conflicts of Interest

The authors declare that they have no conflicts of interest.

Acknowledgments

The authors are extremely grateful to the University of Technology, Iraq, for its outstanding assistance.

References

[1] A. A. Aminuddin Jafry, N. Kasim, Y. Munajat et al., "Passively Q-switched erbium-doped fiber laser utilizing lutetium oxide deposited onto D-shaped fiber as a saturable absorber," *Optik*, vol. 193, Article ID 162792, 2019.

[2] H. Hassan, A. A. Salman, M. A. Munshid, and A. Al-Janabi, "Passive Q-switching using Lead Sulfide suspension as a saturable absorber in 1.5 μm region," *Optical Fiber Technology*, vol. 52, Article ID 101969, 2019.

[3] M. Skorczakowski, J. Swiderski, W. Pichola et al., "Mid-infrared Q-switched Er: YAG laser for medical applications," *Laser Physics Letters*, vol. 7, no. 7, pp. 498–504, 2010.

[4] Y. Okamoto, R. Kitada, Y. Uno, and H. Doi, "Cutting of solid type molded composite materials by Q-switched fiber laser with high-performance nozzle," *Journal of Advanced Mechanical Design, Systems, and Manufacturing*, vol. 2, no. 4, pp. 651–660, 2008.

[5] A. Shakir Al-Hiti, M. Rahman, S. Harun, P. Yupapin, and M. Yasin, "Holmium oxide thin film as a saturable absorber for generating Q-switched and mode-locked erbium-doped fiber lasers," *Optical Fiber Technology*, vol. 52, Article ID 101996, 2019.

[6] H. Hassan, M. A. Munshid, and A. Al-Janabi, "L-band dual-wavelength passively Q-switched erbium-doped fiber laser based on tellurium oxide nanoparticle saturable absorber," *Laser Physics*, vol. 30, no. 2, Article ID 25101, 2020.

[7] M. F. A. Rahman, M. F. M. Rusdi, A. A. Latiff, M. B. Hisyam, K. Dimyati, and S. W. Harun, "Passively Q-switched Erbium-doped fiber laser by incorporating a segment of Thulium-doped fiber saturable absorber," *Journal of Physics: Conference Series*, vol. 1151, Article ID 12010, 2019.

[8] E. I. Ismail, F. Ahmad, S. Ambran, A. A. Latiff, and S. W. Harun, "Q-switched erbium-doped fiber lasers based on copper nanoparticles saturable absorber," *Journal of Physics: Conference Series*, vol. 1371, no. 1, Article ID 12028, 2019.

[9] A. A. Salman and A. Al-Janabi, "Triple-wavelength Q-switched ytterbium-doped fiber laser based on tungsten oxide as saturable absorber," *Microwave and Optical Technology Letters*, vol. 62, no. 6, pp. 2257–2262, 2020.

[10] O. Svelto and D. C. Hanna, *Principles of Lasers*, vol. 1, Springer, New York, NY, USA, 2010.

[11] Q. Bao, H. Zhang, Y. Wang et al., "Atomic-Layer graphene as a saturable absorber for ultrafast pulsed lasers," *Advanced Functional Materials*, vol. 19, no. 19, pp. 3077–3083, 2009.

[12] M. Z. Ab Razak, Z. S. Saleh, F. Ahmad, C. L. Anyi, S. W. Harun, and H. Arof, "High-power Q-switched erbium-ytterbium codoped fiber laser using multiwalled carbon nanotubes saturable absorber," *Optical Engineering*, vol. 55, no. 10, Article ID 106112, 2016.

[13] X. Ban, P. Sun, A. Qyyum et al., "Fe3O4 nanoparticle-enabled Q-switched pulse generation in fiber laser," *Optical Fiber Technology*, vol. 71, Article ID 102909, 2022.

[14] U. Keller, K. J. Weingarten, F. Kärtner, D. Kopf, B. Braun, and I. D. Jung, "Semiconductor saturable absorber mirrors (SESAM's) for femtosecond to nanosecond pulse generation in solid-state lasers," *IEEE Journal of Selected Topics in Quantum Electronics*, vol. 2, no. 3, pp. 435–453, 1996.

[15] Y. Hori, Z. Zhang, and M. Nakazawa, "1070 NM passively mode-locked ytterbium-doped fiber soliton laser with SWNT/PMMA saturable absorber," in *Proceedings of the 17th Microscopics conference (MOC)*, pp. 1-2, IEEE, Sendai, Japan, October 2011.

[16] A. Shakir Al-Hiti, H. Hassan, M. Yasin, and S. Harun, "Passively Q-switched 2 μm fiber laser with WO3 saturable absorber," *Optical Fiber Technology*, vol. 75, Article ID 103193, 2023.

[17] B. Chen, X. Zhang, K. Wu, H. Wang, J. Wang, and J. Chen, "Q-switched fiber laser based on transition metal dichalcogenides MoS_2, MoSe_2, WS_2, and WSe_2," *Optics Express*, vol. 23, no. 20, pp. 26723–26737, 2015.

[18] Z. Luo, Y. Huang, J. Weng et al., "106μm Q-switched ytterbium-doped fiber laser using few-layer topological insulator Bi_2Se_3 as a saturable absorber," *Optics Express*, vol. 21, no. 24, pp. 29516–29522, 2013.

[19] M. F. A. Rahman, A. A. Latiff, A. H. A. Rosol, K. Dimyati, P. Wang, and S. W. Harun, "Ultrashort pulse soliton fiber laser generation with integration of antimony film saturable absorber," *Journal of Lightwave Technology*, vol. 36, no. 16, pp. 3522–3527, 2018.

[20] M. F. Bin Ab Rahman, M. F. Mohd Rusdi, S. Wadi Harun, and M. Yasin, "Q-switched thulium-doped fiber laser using vanadium oxide saturable absorber," *Nonlinear Optics, Quantum Optics*, vol. 48, no. 4, pp. 295–303, 2018.

[21] A. M. Salman, A. Al-Janabi, and P. V. A. Ni-Nps doped, "Ni-NPs doped PVA: an efficient saturable absorber for generation multiwavelength Q-switched fiber laser system near 1.5 μm," *Optical Materials*, vol. 98, Article ID 109418, 2019.

[22] Z. Luo, Y. Li, M. Zhong et al., "Nonlinear optical absorption of few-layer molybdenum diselenide (MoSe_2) for passively

mode-locked soliton fiber laser [Invited]," *Photonics Research*, vol. 3, no. 3, pp. 79–86, 2015.

[23] C. Zhao, H. Zhang, X. Qi et al., "Ultra-short pulse generation by a topological insulator based saturable absorber," *Applied Physics Letters*, vol. 101, no. 21, Article ID 211106, 2012.

[24] H. Yang, X. Feng, Q. Wang et al., "Giant two-photon absorption in bilayer graphene," *Nano Letters*, vol. 11, no. 7, pp. 2622–2627, 2011.

[25] Y. Zhao, A. Dunn, J. Lin, and D. Shi, "Photothermal effect of nanomaterials for efficient energy applications," in *Novel Nanomaterial for Biomedical, Environmental and Engineering Application*, pp. 415–434, Elsevier, Amsterdam, The Netherlands, 2019.

[26] Y. Li, L. Wang, L. Li, and L. Tong, "Optical microfiber-based ultrafast fiber lasers," *Applied Physics B*, vol. 125, pp. 192–210, 2019.

[27] K. Wang, J. Wang, J. Fan et al., "Ultrafast saturable absorption of two-dimensional MoS_2 n," *ACS Nano*, vol. 7, no. 10, pp. 9260–9267, 2013.

[28] R. Febrida, S. Setianto, E. Herda, A. Cahyanto, and I. M. Joni, "Structure and phase analysis of calcium carbonate powder prepared by a simple solution method," *Heliyon*, vol. 7, no. 11, Article ID 8344, 2021.

[29] I. Schmidt and W. Wagermaier, "Tailoring calcium carbonate to serve as optical functional material: examples from biology and materials science," *Advanced Materials Interfaces*, vol. 4, no. 1, Article ID 1600250, 2017.

[30] T. Pascal, U. Adam, and J. C. Ododo, "The phenomenon of nonlinear optical birefringence in uniaxial crystals," *Latin-American Journal of Physics Education*, vol. 5, no. 2, p. 19, 2011.

[31] A. S. Zulkhairi, S. R. Azzuhri, and R. A. Shaharuddin, "Switchable multiwavelength ytterbium-doped fiber laser using a non-adiabatic microfiber interferometer," *Laser Physics*, vol. 27, no. 5, Article ID 55104, 2017.

[32] R. Chi, K. Lu, and S. Chen, "Multi-wavelength Yb-doped fiber-ring laser," *Microwave and Optical Technology Letters*, vol. 36, no. 3, pp. 170–172, 2003.

[33] F. Rashid, S. Razalli, M. A. Mat Salim et al., "Using a black phosphorus saturable absorber to generate dual wavelengths in a Q-switched ytterbium-doped fiber laser," *Laser Physics Letters*, vol. 13, no. 8, Article ID 851023, 2016.

[34] S. Biradar, P. Ravichandran, R. Gopikrishnan et al., "Calcium carbonate nanoparticles: synthesis, characterization, and biocompatibility," *Journal of Nanoscience and Nanotechnology*, vol. 11, no. 8, pp. 6868–6874, 2011.

[35] S. Srivastava and P. K. Varshney, "A structural study of mixed ion PVA based composite polymer electrolyte using x-ray diffraction studies," *International Journal of Applied Engineering Research ISSN*, vol. 12, no. 11, pp. 2926–2928, 2017.

[36] D. Wang, Z. Zhang, Q. Yuan, Z. Dong, and C. Xiao, "The isothermal crystallization kinetics of ethyl cellulose/poly (ethylene oxide)/ethyl cellulose sandwich films," *Journal of Polymer Research*, vol. 17, no. 5, pp. 745–750, 2010.

[37] G. W. C. Kaye and T. Howell Laby, "Tables of physical and chemical constants and some mathematical functions," *Longmans, Green and Company*, vol. 40, no. 7, p. 938, 1926.

[38] R. Ranjan, S. D. Narnaware, and N. V. Patil, "A novel technique for synthesis of calcium carbonate nanoparticles," *National Academy Science Letters*, vol. 41, no. 6, pp. 403–406, 2018.

[39] J. Aufort and R. Demichelis, "Magnesium impurities decide the structure of calcium carbonate hemihydrate," *Crystal Growth & Design*, vol. 20, no. 12, pp. 8028–8038, 2020.

[40] A. Ghadami Jadval Ghadam and M. Idrees, "Characterization of $CaCO_3$ nanoparticles synthesized by reverse microemulsion technique in different concentrations of surfactants," *Iranian Journal of Chemistry and Chemical Engineering (International English Edition)*, vol. 32, no. 3, pp. 27–35, 2013.

[41] M. M. Khalil, A. H. El-Sayed, M. S. Masoud, E. M. Mahmoud, and M. A. Hamad, "Synthesis and optical properties of alizarin yellow GG-Cu(II)-PVA nanocomposite film as a selective filter for optical applications," *Journal of Materials Research and Technology*, vol. 11, pp. 33–39, 2021.

[42] Y. Ramadin, M. Al-Haj Abdallah, M. Ahmad, A. Zihlif, S. Al-Ani, and S. Al-Ani, "Optical properties of epoxy-glass microballoons composite," *Optical Materials*, vol. 5, no. 1-2, pp. 69–73, 1996.

[43] S. N. Alhosseini, F. Moztarzadeh, M. Mozafari et al., "Synthesis and characterization of electrospun polyvinyl alcohol nanofibrous scaffolds modified by blending with chitosan for neural tissue engineering," *International Journal of Nanomedicine*, vol. 7, pp. 25–34, 2012.

[44] D. Jahani, N. Amin, J. Ghourbanpour, and A. Ameli, "Polyvinyl alcohol/calcium carbonate nanocomposites as efficient and cost-effective cationic dye adsorbents," *Polymers*, vol. 12, no. 10, Article ID 110728, 2020.

[45] A. H. Abdalhadi, A. M. Salman, R. A. Faris, and A. Al-Janabi, "Titania-carbon nanocomposite as a saturable absorber for generation passively ytterbium-mode locked pulses," *Optical Materials*, vol. 112, Article ID 110728, 2021.

[46] S. Arun Kumar, J. Senthilselvan, and G. Vinitha, "Third-order nonlinearity and optical limiting behaviors of Yb: YAG nanoparticles by Z-scan technique," *Optics & Laser Technology*, vol. 109, pp. 561–568, 2019.

[47] H. Hassan, M. A. Munshid, and A. Al-Janabi, "Tellurium-nanorod-based saturable absorber for an ultrafast passive mode-locked erbium-doped fiber laser," *Applied Optics*, vol. 59, no. 4, pp. 1230–1236, 2020.

[48] H. Ahmad, M. F. Ismail, S. N. M. Hassan, F. Ahmad, M. Z. Zulkifli, and S. W. Harun, "Multiwall carbon nanotube polyvinyl alcohol-based saturable absorber in passively Q-switched fiber laser," *Applied Optics*, vol. 53, no. 30, pp. 7025–7029, 2014.

[49] H. Hassan, M. A. Munshid, and A. Al-Janabi, "Four-wave-mixing assisted multi-wavelength short pulse generation in an erbium-doped-fiberlaser-based tellurium nanorod saturable absorber," *Photonics and Nanostructures: Fundamentals and Applications*, vol. 43, Article ID 100884, 2021.